Ocean Engineering 340 (2025) 122195

Contents lists available at ScienceDirect

Ocean Engineering

journal homepage: www.elsevier.com/locate/oceaneng

Research paper

Simulation of solitary wave generation and wave-structure interactions using an MPM-SDEM coupling scheme

Songkai Ren[a,b,1], Zhuo Liu[c,d,1], M.G. Trujillo-Vela[e,f], S.A. Galindo-Torres[d], Xiaoqing Tian[a,b,*], Pei Zhang[g]

[a] School of Mechanical Engineering, Hangzhou Dianzi University, Hangzhou, 310018, Zhejiang, China
[b] International Co-Operation Platform of Intelligent Ocean Equipments Technology of Zhejiang Province, Hangzhou Dianzi University, Hangzhou, 310018, Zhejiang, China
[c] Department of Earth and Planetary Science, University of California, Berkeley, CA, 94720, USA
[d] School of Engineering, Westlake University, Hangzhou, 310024, Zhejiang, China
[e] Faculty of Engineering, Universidad Surcolombiana, Avenue Pastrana Borrero, Carrera 1, Neiva, 410001, Huila, Colombia
[f] Gea Tekhne, Calle 164 No. 16C - 15, Bogotá, D.C., 110131054, Colombia
[g] School of Energy and Power Engineering, Nanjing University of Science and Technology, Jiangsu, China

ARTICLE INFO

Keywords:
Material point method
Discrete element method
Wave-structure interaction
Hydrodynamic loading

ABSTRACT

Accurately simulating the interaction of solitary waves with seawalls poses a significant challenge for existing numerical methods, primarily due to the complexities associated with large free-surface deformations and intricate fluid-structure interactions. To address these challenges, this study proposes a coupled framework combining the Material Point Method (MPM) with Spheropolygon Discrete Element Method (SDEM) for simulating the generation of solitary waves and their interactions with seawalls. The coupling is achieved by detecting collisions between MPM and SDEM particles and computing contact forces using an elastic dash-pot model, enabling dynamic momentum exchange. Validation of the coupled framework is conducted through several benchmark cases, including solitary wave propagation in flat flumes, run-up height on vertical walls, and impact load measurements. The results demonstrate that the proposed method reliably captures free-surface behavior, wave velocities, and hydrodynamic loading in agreement with experimental and theoretical results. The framework is subsequently applied to perform a detailed analysis of solitary wave-structure interactions for different slopes, revealing how wave velocity and hydrodynamic loads evolve over time and how they correlate with wave breaking, run-up, and reflection processes.

1. Introduction

Extreme wave events, such as those triggered by tsunamis, pose significant threats to coastal infrastructure and nearshore regions (Meucci et al., 2020). For example, the Tohoku-Oki tsunami in Japan resulted in approximately 18,000 fatalities (Takashimizu et al., 2020). Solitary waves are frequently employed in both numerical and experimental models to study tsunami events due to their analogous shapes and intrinsic hydrodynamic properties (Yao et al., 2018; Wang et al., 2018; Zhao et al., 2021). It is important to note that solitary waves fail to capture essential tsunami features, particularly when the wave front steepens into an undular bore, which can lead to significant errors in the predicted flow depth, arrival time, and force distribution (Madsen et al., 2008). In addition, accurately simulating solitary wave dynamics remains challenging due to the complexity of wave generation, propagation, free-surface evolution, and interaction with coastal structures.

Laboratory experiments are crucial for investigating wave propagation and wave-structure interactions. Hsiao et al. (2008) examined the run-up of solitary waves on various slopes and proposed a formula to predict the maximum run-up height. Krautwald et al. (2022) conducted a series of experiments in a large wave flume to evaluate impact forces on elevated buildings. Nevertheless, experimental studies are often expensive and may introduce inherent uncertainties due to scale effects (Heller, 2011; Man et al., 2023).

Numerical methods offer alternative approaches for studying the complex phenomena described above. Jose et al. (2017) implemented both the Finite Difference and Finite Volume Methods to investigate wave interactions with offshore structures. However, these approaches

* Corresponding author.
E-mail address: tianxiaoqing@hdu.edu.cn (X. Tian).
[1] These authors contributed equally to this work.

https://doi.org/10.1016/j.oceaneng.2025.122195
Received 24 April 2025; Received in revised form 11 July 2025; Accepted 11 July 2025

may be inadequate for simulating free-surface waves, as they require specialized techniques to accurately track the evolving free-surface (Han and Dong, 2020; Vacondio et al., 2021). Smoothed Particle Hydrodynamics (SPH) is a competitive meshless approach for analyzing free-surface flows. It discretizes the domain into particles, making it ideal for modeling problems with changing shapes (Luo et al., 2021; Lind et al., 2020). Therefore, Altomare et al. (2023) used SPH to reproduce wave breaking over a barred beach, validating their results against experimental data. Several variants of this meshless approach have been implemented to study shoreline interaction problems. For instance, δ-SPH has been used to study how solitary waves interact with marine structures. Results show that the geometry and placement of deck protrusions significantly affect this interaction (Fu et al., 2024). Additionally, the Moving Particle Semi-Implicit Method (MPS) has been applied to simulate solitary waves overtopping a sloping seawall. It is capable of accurately reproducing the entire propagation process of solitary waves, including run-up, run-down, and potential hydraulic jump phenomena (He et al., 2021). In these methods, the wall-potential particles were implemented to simulate paddle motion, retaining the properties of fluid particles but with velocity directions opposite to those of the fluid. In MPS and SPH methods, alternative wave generation techniques like internal wave makers (Liu et al., 2015) or wavy interface approaches (Tsuruta et al., 2021; Shimizu and Gotoh, 2024) have drawbacks. Internal wave makers increase computational time, while wavy interface approaches suffer from compromised wave production when reflections occur. Unlike the velocity boundary based wave generation method, this study employs an DEM based localized force-driven mechanism to initiate wave motion directly within the fluid domain. This method offers several advantages, including reduced computational overhead, and enhanced integration with particle-based solvers.

Coupling schemes are also strategically effective for modeling interactions between waves and coastal structures. Sun et al. (2024a) employed a coupled Smoothed Particle Hydrodynamics-Discrete Element Method (SPH-DEM) solver to analyze the dynamic behavior of breakwaters under rapid flow impact. Furthermore, Tsuruta et al. (2019) used an SPH-DEM coupling approach to study dam-break problems with porous media and tsunami-induced scour. However, this method introduces pseudo-friction in the pressure gradient because it only considers velocity components in the normal direction. Moreover, SPH methods encounter challenges in handling boundary conditions due to incomplete particle support near boundaries and face challenges with the efficiency of their neighbor-finding algorithms (Tsuruta et al., 2021; Domínguez et al., 2019; Ren et al., 2023a).

To overcome these limitations, this study developed a coupled Material Point Method- Spheropolygon DEM (MPM-SDEM) numerical framework for the effective simulation of solitary wave generation and its interaction with coastal structures. The normal and tangential contact forces between the MPM and SDEM components are resolved using an elastic spring-dashpot model, providing a more physically realistic representation of the interaction dynamics. The MPM offers a promising alternative by employing both mesh and particle discretization (Kularathna et al., 2021; De Vaucorbeil et al., 2020; Ni et al., 2022). In the MPM, a set of moving points represents the computational domain over a fixed mesh. This avoids mesh distortion and eliminates the need for neighbor searching among particles, as the background mesh connectivity determines interactions (Lei et al., 2022). Zhang et al. (2017) successfully used MPM to model free-surface flows. They effectively addressed pressure oscillations, allowing for accurate simulations of dam-break flows, droplet dynamics, and fluid-structure interactions. Similarly, Sun et al. (2024b) introduced a density-smoothing B-spline MPM to simulate dam-break flows, water impacts on elastic obstacles, and the water entry of solid objects. Their method showed high accuracy in capturing complex fluid behavior and structural responses. However, it is noteworthy that these studies primarily focus on flow phenomena driven by gravitational forces, with limited application to wave-dominated scenarios. Harris et al. (2021) employed the MPM approach to evaluate the run-up responses of incident solitary waves on vertical permeable seawalls and sloped permeable beaches, emphasizing the influence of permeability on solitary wave run-up.

The dual mesh-particle framework of MPM facilitates seamless coupling with other numerical methods (Zhao et al., 2020; Shi et al., 2024; Li et al., 2023), making it suitable for studying interactive phenomena. MPM has been effectively coupled with the Finite Element Method (FEM) to model the intricate interactions between granular materials and water (Pan et al., 2021). However, the accurate capture of free-surface dynamics within the FEM framework requires coupling with a phase-field method. Lei et al. (2024) developed a new MPM-FEM hybrid model to analyze the hydrodynamic response of a triangular semi-submersible platform under wave loading, demonstrating that wave incidence angles significantly impact platform motions and mooring line tensions. Recently, the unified DEM-MPM coupling approach has been proposed for simulating soil-rock interactions (Shi et al., 2024; Li et al., 2023; Zhao et al., 2020). Nevertheless, its applications in fluid-structure interactions, particularly concerning seawalls, remain limited.

This paper is organized as follows: Section 2 introduces the wave generation theory. Section 3 provides a comprehensive overview of MPM, DEM, and their coupling approach. Sections 4 and 5 present validation cases and application examples, respectively. Finally, Section 6 summarizes the key contributions of this work.

2. Paddle-type wave-maker principle

A paddle-type wave maker is one of the most widely used methods for generating solitary waves. Fig. 1 illustrates the generation and propagation of a solitary wave using this setup. The paddle velocity is defined as equal to the depth-averaged horizontal water particle velocity, as given by Goring's formulation (Goring and Raichlen, 1979), shown in Eq. (1):

$$\frac{dX}{dt} = \bar{u}(X,t), \tag{1}$$

where X denotes the position of the wave-maker at time t. The depth-averaged velocity is given by Eq. (2) (Svendsen, 1974):

$$\bar{u}(X,t) = \frac{c\,\eta(X,t)}{d+\eta(X,t)}, \tag{2}$$

where c represents the wave celerity, d is the still water depth, and $\eta(X,t)$ denotes the free surface elevation. Combining Eqs. (1) and (2), and integrating the result, yields the paddle displacement equation, defined as follows:

$$X(t) = \frac{2h}{kd}\tanh\left[k\left(c\,t - X\right)\right], \tag{3}$$

where h is the wave height and k is the outskirt coefficient. The solitary wave profile is described by:

$$\eta(X,t) = 2h\,\mathrm{sech}^2\left[k\left(c\,t - X\right)\right]. \tag{4}$$

The solution to the two above implicit equations is provided through the Korteweg-de Vries (KdV) formulation, which describes first-order shallow water dynamics (Domínguez et al., 2019; Korteweg and de Vries,

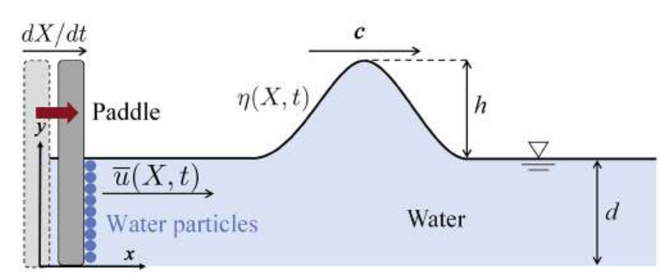

Fig. 1. Generation and propagation of a solitary wave in a constant water depth.

1895). Accordingly, the paddle displacement equation is given by:

$$X(t) = 2\sqrt{\frac{hd}{3}}\left\{1+\tanh\left[k\,c_{KdV}\left(t-\frac{T_f}{2}\right)\right]\right\}, \tag{5}$$

where the outskirt coefficient k, the wave celerity c_{KdV}, and the generation time T_f are defined as follows:

$$\begin{aligned} k &= \sqrt{\frac{3h}{4d^3}}, \\ c_{KdV} &= \sqrt{gd}\left(1+\frac{h}{2d}\right), \\ T_f &= \frac{2}{k\,c_{KdV}}\left(3.8+\frac{h}{d}\right). \end{aligned} \tag{6}$$

Consequently, the theoretical surface elevation given by Eq. (4) can be rewritten as follows:

$$\eta(X,t) = h\,\mathrm{sech}^2\left\{k\left[c\left(t-\frac{T_f}{2}\right)+2\sqrt{\frac{h\,d}{3}}-X\right]\right\}. \tag{7}$$

3. Numerical methodology

3.1. Material point method for water

The MPM is a hybrid numerical technique that combines the advantages of both mesh-based and particle-based methods, which is particularly effective for simulating water flows undergoing large deformations (Ni et al., 2022). In MPM, a continuous body is discretized into a set of material points that hold all historical information, which eliminates issues with mesh distortion. Temporary data is stored on background nodes, which are then used to solve the following governing equations (Lei et al., 2022):

$$\frac{D\rho_f}{Dt} = -\rho_f \nabla\cdot \boldsymbol{v}_f, \tag{8}$$

$$\rho_f \frac{D\boldsymbol{v}_f}{Dt} = \nabla\cdot\boldsymbol{\sigma}_s + \rho_f \boldsymbol{b}_f - \boldsymbol{F}^c, \tag{9}$$

where ρ_f and $\boldsymbol{v}_f$ denote the fluid density and velocity, respectively, $\boldsymbol{\sigma}_s$ represents the Cauchy stress tensor, $\boldsymbol{b}_f$ denotes the body force, and $\boldsymbol{F}^c$ is the coupling force. $D()/Dt = \partial()/\partial t + \boldsymbol{v}_f\cdot\nabla()$ represents the Lagrangian or material derivative. The fluid is assumed to be weakly compressible so that the pressure can be related to the density through an equation of state (Zhao et al., 2019; Sun et al., 2024b). In the subsequent formulations, the point and nodal values are denoted using the subscripts p and i, respectively.

(a) Physical information is transferred from points to nodes at the current time step t, the nodal quantities, specifically nodal mass m_i^t, momentum $m_i^t\boldsymbol{v}_i^t$, external force $\boldsymbol{f}_i^{\mathrm{ext},t}$, and internal force $\boldsymbol{f}_i^{\mathrm{int},t}$, are computed by mapping the corresponding values from the material points.

$$m_i^t = \sum_p m_p^t S_{ip}, \tag{10}$$

$$m_i^t\boldsymbol{v}_i^t = \sum_p m_p^t \boldsymbol{v}_p^t S_{ip}, \tag{11}$$

$$\boldsymbol{f}_i^{\mathrm{ext},t} = \left(\boldsymbol{F}_p^{c,t} + \sum_p \boldsymbol{b}^t m_p^t\right) S_{ip}, \tag{12}$$

$$\boldsymbol{f}_i^{\mathrm{int},t} = -\sum_p \mathcal{V}_p^t \boldsymbol{\sigma}_p^t \nabla S_{ip}, \tag{13}$$

where m_p^t and $\boldsymbol{v}_p^t$ represent the mass and velocity of the material point, respectively. $\boldsymbol{b}^t$, $\mathcal{V}_p^t$, and $\boldsymbol{\sigma}_p^t$ denote the body force, volume, and Cauchy stress tensor at the material point, respectively. $\boldsymbol{F}_p^{c,t}$ is the contact force used to couple MPM framework with the DEM solver. $S_{ip} = S_i(\boldsymbol{x}_p)$ is the weighting function of node i that is evaluated at the point's position $\boldsymbol{x}_p$. It is well known that the original MPM weighting function is prone to cell-crossing errors. To mitigate these numerical inaccuracies, this study employs the Generalized Interpolation Material Point Method (GIMP) to replace the original weighting function (Bardenhagen and Mm, 2004).

(b) The governing equations are solved at the grid nodes by evaluating:

$$\boldsymbol{v}_i^{t+\Delta t} = \frac{\left(\boldsymbol{f}_i^{\mathrm{ext},t} + \boldsymbol{f}_i^{\mathrm{int},t}\right)\Delta t}{m_i^t} + \boldsymbol{v}_i^t. \tag{14}$$

Essential boundary conditions are imposed at this stage, and Δt is the time increment.

(c) Physical information is transferred from grid nodes back to the points. Subsequently, the positions and velocities of the points are updated:

$$\boldsymbol{x}_p^{t+\Delta t} = \boldsymbol{x}_p^t + \Delta t \sum_i \boldsymbol{v}_i^t S_{ip}, \tag{15}$$

$$\boldsymbol{v}_p^{t+\Delta t} = \boldsymbol{v}_p^t + \Delta t \sum_i \left(\frac{\boldsymbol{f}_i^{\mathrm{ext},t} + \boldsymbol{f}_i^{\mathrm{int},t}}{m_i^t}\right) S_{ip}. \tag{16}$$

(d) The strain, vorticity, and stress tensors, as well as the fluid pressure, are updated at the material points. The strain increment rate tensor $\dot{\boldsymbol{\varepsilon}}_p^{t+\Delta t}$ and vorticity increment rate tensor $\dot{\boldsymbol{\omega}}_p^{t+\Delta t}$ are computed from the updated nodal velocity field:

$$\dot{\boldsymbol{\varepsilon}}_p^{t+\Delta t} = \frac{1}{2}\sum_i \left[\nabla S_{ip}\boldsymbol{v}_i^{t+\Delta t} + \left(\nabla S_{ip}\boldsymbol{v}_i^{t+\Delta t}\right)^T\right], \tag{17}$$

$$\dot{\boldsymbol{\omega}}_p^{t+\Delta t} = \frac{1}{2}\sum_i \left[\nabla S_{ip}\boldsymbol{v}_i^{t+\Delta t} - \left(\nabla S_{ip}\boldsymbol{v}_i^{t+\Delta t}\right)^T\right], \tag{18}$$

where ∇S_{ip} is the gradient of the weighting function. The density $\rho_p^{t+\Delta t}$ at the material point is updated based on the strain increment tensor $\Delta\boldsymbol{\varepsilon}_p^t = \dot{\boldsymbol{\varepsilon}}_p^t \Delta t$:

$$\rho_p^{t+\Delta t} = \frac{\rho_p^t}{1+\mathrm{tr}\left(\Delta\boldsymbol{\varepsilon}_p^{t+\Delta t}\right)}. \tag{19}$$

where tr denotes the trace of the strain increment tensor. Since the point mass m_p is constant for a Lagrangian point, the volume $\mathcal{V}_p^{t+\Delta t}$ is updated as:

$$\mathcal{V}_p^{t+\Delta t} = \left[1+\mathrm{tr}\left(\Delta\boldsymbol{\varepsilon}_p^{t+\Delta t}\right)\right]\mathcal{V}_p^t. \tag{20}$$

Subsequently, the Cauchy stress tensor $\boldsymbol{\sigma}_p^{t+\Delta t}$ is updated based on the vorticity and strain rate tensors:

$$\boldsymbol{\sigma}_p^{t+\Delta t} = \boldsymbol{\sigma}_p^t + \dot{\boldsymbol{\sigma}}_p^t\left(\dot{\boldsymbol{\omega}}_p^t, \dot{\boldsymbol{\varepsilon}}_p^t\right)\Delta t. \tag{21}$$

For fluids, the Cauchy stress tensor can be decomposed as follows (Chen et al., 2018):

$$\boldsymbol{\sigma}_p^t = p_p^t\mathbf{I} + 2\mu\dot{\boldsymbol{\varepsilon}}_p^{\mathrm{dev},t}, \tag{22}$$

where μ is the dynamic viscosity, $\dot{\boldsymbol{\varepsilon}}_p^{\mathrm{dev},t}$ is the deviatoric strain rate tensor, $\mathbf{I}$ is the identity tensor, and p_p^t denotes the fluid pressure. When weak compressibility is allowed, the fluid pressure is estimated using an equation of state, such as Monaghan (1994):

$$p_p^t = \frac{\rho^0 C_s^2}{\gamma}\left[\left(\frac{\rho_p^t}{\rho^0}\right)^\gamma - 1\right], \tag{23}$$

where C_s is the speed of sound, which is typically set at least ten times the anticipated maximum fluid velocity to restrict the density variation down to 1 % (Monaghan, 2005). ρ^0 and ρ_p^t are the reference and current density, and $\gamma = 7$ for water. Finally, the nodal information is reset in preparation for the subsequent computational cycle.

It is noted that the current MPM formulation does not explicitly incorporate a turbulence model. This study adopts the same governing equations as previous particle-based approaches (Zhao et al., 2019; He et al., 2021; Chen et al., 2024) to ensure a fair comparison between numerical methods. Nevertheless, the framework can be extended to incorporate turbulence effects through an turbulence viscosity based model as demonstrated in previous work (King et al., 2023).

3.2. Spheropolygon discrete element method for paddle

The Spheropolygonal DEM (SDEM) is used to model the paddle due to its capacity to approximate complex geometries using spheropolygons and simplify collision handling with spherical elements. The core principle of SDEM involves first eroding the object using a pre-defined sphere and then dilating the eroded shape with the same sphere. This process yields a geometrically similar representation of the original object, but with rounded corners. As a result, irregular shapes can be represented with continuous boundaries, facilitating collision handling (Galindo-Torres et al., 2012). Translational (Eq. (24)) and rotational (Eq. 25) motions are considered to describe the dynamics of DEM particles (Zhang et al., 2022):

$$m_i \boldsymbol{a}_i = m_i \boldsymbol{g} + \sum_{j=1}^{N} \boldsymbol{f}_{ij} + \boldsymbol{F}^{\mathrm{c}}, \tag{24}$$

$$\frac{d}{dt}(\boldsymbol{I}_i \boldsymbol{w}_i) = \sum_{j=1}^{N} \boldsymbol{t}_{ij} + \boldsymbol{T}^{\mathrm{c}}, \tag{25}$$

In this framework, m_i and $\boldsymbol{a}_i$ denote the mass and acceleration of particle i, respectively. $\boldsymbol{I}_i$ is the moment of inertia of the DEM particle, and $\boldsymbol{w}_i$ represents its angular velocity. $m_i\boldsymbol{g}$ correspond to the gravitational force, while $\boldsymbol{f}_{ij}$ and $\boldsymbol{t}_{ij}$ denote the contact force and torque coming from DEM interactions, respectively. The torque induced by the coupling force, $\boldsymbol{F}^{\mathrm{c}}$, from the MPM solver is represented by $\boldsymbol{T}^{\mathrm{c}}$.

3.3. Coupling between MPM and SDEM

Collision detection and contact force calculation are essential components of the coupling algorithm. This study implements a DEM-based coupling strategy to compute the interactions between MPM and DEM particles. Specifically, MPM points are temporarily treated as DEM particles during interactions in order to compute the coupling force.

3.3.1. Collision detection

A circular region surrounding the SDEM particle is first used to identify the affected MPM nodes, as illustrated in Fig. 2. The radius of this circle, R_{circle}, consists of three components:

$$R_{\mathrm{circle}} = r_{\mathrm{dem}} + r_{\mathrm{sphero}} + r_{\mathrm{extend}}, \tag{26}$$

where r_{dem} is the maximum distance from the centroid to any point on the edge of a SDEM particle, r_{sphero} represents the radius of the sphere, and r_{extend} is an additional radius used to ensure that a sufficient number of nodes are considered for potential contact. Then, MPM information is transferred from material points to grid nodes, enabling evaluation of whether the nodes influenced by SDEM particles are activated by MPM points as well. If a node is affected by both entities, the corresponding SDEM particle and MPM point are flagged as a potential contact pair and added to the contact list for further examination. Once the potential contact list is established, the next step is to compute the geometric overlap between two entities to verify if a collision has occurred:

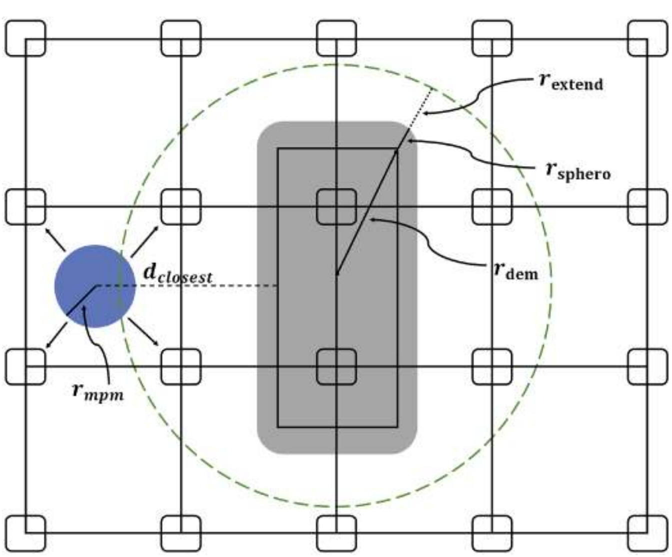

Fig. 2. Collision detection between MPM and SDEM particles.

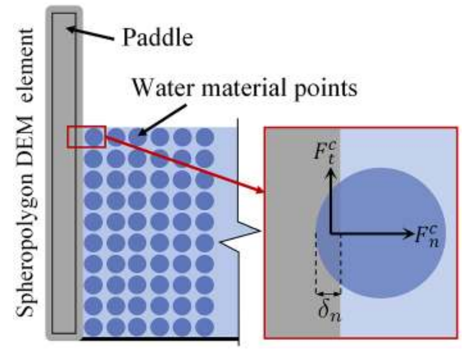

Fig. 3. Contact force calculation for paddle and water MPM.

$$\delta = r_{\mathrm{sphero}} + r_{\mathrm{mpm}} - d_{\mathrm{closest}}, \tag{27}$$

where d_{closest} represents the Euclidean distance from the material point to the edge of the SDEM particle, and r_{mpm} denotes the radius of the material point, which is derived from the circle that has an equivalent area to the original control domain of GIMP.

3.3.2. Contact force calculation

Contact force is calculated within the DEM framework, as shown in Fig. 3. The contact law is derived under the assumption of an elastic collision between two particles. In this context, the linear spring-dashpot model is implemented to compute the coupling force. The normal force and tangential force are defined as follows (Luding, 2008):

$$\boldsymbol{F}_n^{\mathrm{c}} = k_n \delta_n \boldsymbol{n} + g_n \boldsymbol{v}_n, \tag{28}$$

$$\boldsymbol{F}_t^{\mathrm{c}} = -g_t \boldsymbol{v}_t, \tag{29}$$

where k_n and g_n are the normal spring stiffness and damping coefficient, respectively. The parameter δ_n denotes the geometrical overlap, $\boldsymbol{n}$ is the normal unit vector, and $\boldsymbol{v}_n$ represents the relative normal velocity. Similarly, g_t and $\boldsymbol{v}_t$ are the tangential damping coefficient and relative tangential velocity at the contact point. It is also important to note that the relative tangential displacement is constrained to zero to ensure a non-slipping boundary condition. Consequently, only the viscous component, $g_t\boldsymbol{v}_t$, is retained for the tangential contact force.

3.4. Implementation processes

Fig. 4 illustrates the complete numerical procedure from the n^{th} to the $(n+1)^{\mathrm{th}}$ time step. Initially, through the collision detection method, the potential contact list is determined, and the coupling forces between material points and SDEM particles are computed by Eqs. (28) and (29). Then, this computed force, $\boldsymbol{F}^{\mathrm{c}}$, is considered external force and added into the governing equations of SDEM. Finally, within the MPM framework, the coupling force is added into the governing equation of MPM, and the remaining physical quantities are obtained by solving equations from Eqs. (10) to (23).

In this coupling approach, the MPM and DEM solutions are integrated using explicit schemes, and both components adopt the same time step (Liu et al., 2018). To maintain numerical stability, the global time step Δt is constrained by the Courant-Friedrichs-Lewy (CFL) condition

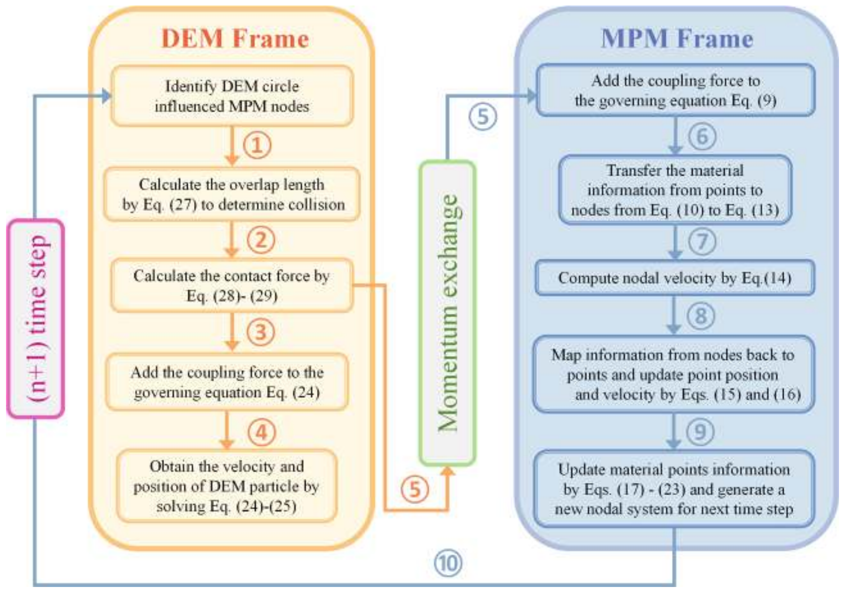

Fig. 4. Flow chart of the numerical process.

(Shi et al., 2024):

$$\Delta t = \kappa \min\left(\frac{h_s}{C_s}, \sqrt{\frac{m}{k_n}}\right) \tag{30}$$

where κ is the Courant number, h_s is the initial size of the material point, C_s is the speed of sound, m is the DEM particle mass, and k_n is the contact normal stiffness. The first term in Eq. (30) corresponds to the MPM, while the second term corresponds to the DEM component.

The parallel algorithms have been developed for the MPM and DEM modules, utilizing an OpenMP framework to maximize high-performance computing resources. The scalability of the framework is enhanced by its foundation on the open-source ComFluSoM library, which supports integration with other existing algorithms like Lattice Boltzmann Method and Random Walk Method (Zhang et al., 2021, 2022), further broadening its application scope for future research.

4. Validation

In this section, four different benchmarks are used to verify the accuracy of the numerical model in predicting wave propagation and wave-structure interactions. Table 1 summarizes the key characteristics of each validation case, offering a clear overview of their respective scopes.

4.1. Solitary wave propagation over a flat bed

Numerical wave flumes are established based on the physical experiments conducted by Liu et al. (2023). As shown in Fig. 5, the flume is 15 m long with a water depth of 0.2 m. Four wave gauges (G1, G2, G3, and G4) are positioned sequentially along the x-axis. A piston-type wave maker, modeled via SDEM, is placed at the left of the flume to generate a solitary wave with a height of 0.1 m. The water is modeled using MPM, the mesh resolution is $0.01\ \mathrm{m} \times 0.01\ \mathrm{m} \times 0.01\ \mathrm{m}$, and particle resolution is 4 per cell. The numerical simulations run on Intel Core™ i9-14900K (10 cores), which took about 1.44 h of runtime.

Table 1
Summary of the geometric configurations used in the validation cases.

Case number	Case 1	Case 2
Flume length (m)	15	15
Water depth (m)	0.2	0.2
Wave height (m)	0.1	0.1
Validated aspect	Surface elevations	Velocity distribution
Comparison data	Experimental	Analytical
Case number	**Case 3**	**Case 4**
Flume length (m)	2.5	2.5
Water depth (m)	0.2	0.2
Wave height (m)	Various	Various
Validated aspect	Run-up height	Impact force
Comparison data	Experimental and numerical	Experimental and semi-analytical

Table 2
Mechanical parameters used in the numerical simulations.

Parameter	Units	Value
MPM		
Density, ρ^{MPM}	kg/m^3	1000
Viscosity, μ	Pa·s	1.0×10^{-3}
SDEM		
Density, ρ^{DEM}	kg/m^3	2000
Sphero-radius, R_s	m	2.0×10^{-3}
Coupling		
Normal stiffness, k_n	kg/s^2	375
Normal damping coefficient, g_n	kg/s	0.15
Tangential damping coefficient, g_t	kg/s	5.0×10^{-6}

The mechanical coefficients employed in this simulation are detailed in Table 2. To determine appropriate values for these parameters, extensive simulations were conducted using a range of material properties until a satisfactory match with the desired result. The sensitivity analysis on the key contact parameters was performed in Section 4.3. Once these parameters have been established through validation, they remain consistent for all subsequent cases involving the same materials.

Fig. 6 compares the numerical wave surface elevations with the experimental data at various gauge locations. It is observed that the wave height slightly decreases during propagation in the experimental results, likely due to frictional effects from the flume walls. The viscous coupling force was accounted in the numerical simulation, resulting in good agreement with the experimental data.

Another notable characteristic in Fig. 6 is the presence of small fluctuations or corrugations in the numerical wave profile as the wave reaches the gauge locations. This behavior results from the compression of certain particles by the paddle during the initial wave generation process, leading to discontinuities in the vertical positions between adjacent particles.

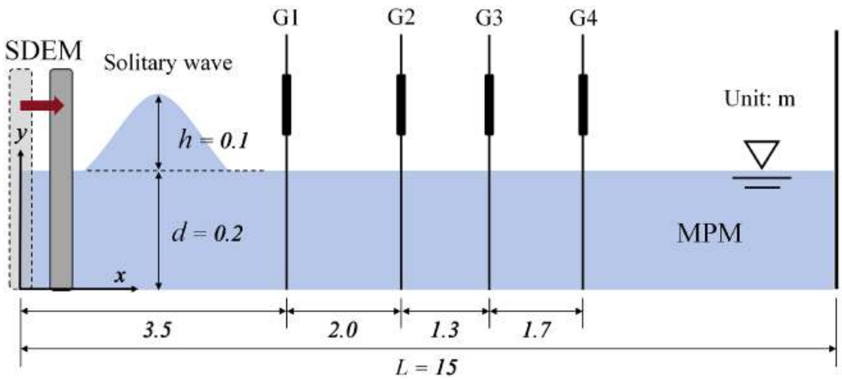

Fig. 5. Layout of the four wave gauges in the flume.

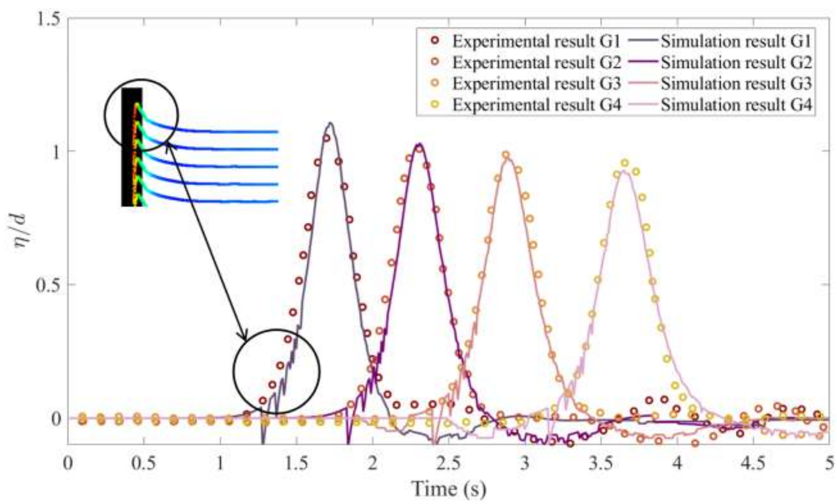

Fig. 6. Numerical results and experimental data of wave surface elevations.

MPM is sensitive to both mesh and particle resolution. Its convergence has been demonstrated in numerous previous studies (Tao et al., 2016; Bardenhagen and Mm, 2004; Bisht et al., 2021), which show that MPM achieves at least first-order accuracy. In the coupling algorithm, the authors have shown in their previous work that employing a finer mesh leads to improved simulation results (Ren et al., 2022). Moreover, when the particles per cell (PPC) value is low, the resolution is insufficient to capture detailed physical interactions around DEM particles. Conversely, a higher PPC intensifies the well-known crossing error (Ren et al., 2023b). Therefore, an optimal PPC of 8 for 3D simulations (4 for 2D) is recommended, as also suggested by other MPM coupling studies (Lian et al., 2012).

An error metric has been incorporated to quantitatively compare the numerical and experimental data. The root mean square error (RMSE) and Percent Deviation are calculated using the following equations:

$$\text{RMSE} = \sqrt{\frac{1}{N}\sum_{i=1}^{N}(S_i - E_i)^2} \tag{31}$$

$$\text{Percent Deviation} = \frac{1}{N}\sum_{i=1}^{N}\left|\frac{S_i - E_i}{E_i}\right| \times 100\,\% \tag{32}$$

where S_i is the simulated value and E_i is the experimental or analytical value, N is the amount of points to perform the error analysis.

As shown in Fig. 7, the RMSE values from Gauges 1 to 4 are 0.0106, 0.0053, 0.0079, and 0.0117, respectively, with corresponding percent deviations of 1.33 %, 0.52 %, 0.88 %, and 1.12 %. Gauge 2 exhibits the lowest error, while Gauges 1 and 4 show slightly higher discrepancies, likely due to proximity to the wave generation and reflection regions.

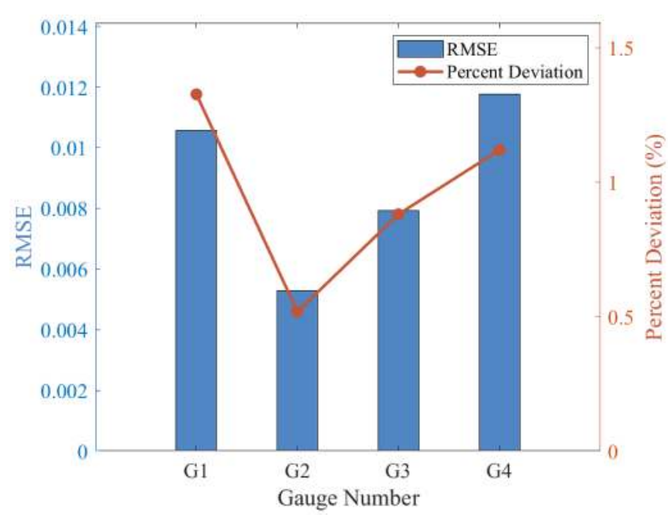

Fig. 7. RMSE and percent deviation of solitary wave propagation over a flat bed.

The RMSE and percent deviation exhibit consistent trends across gauges, supporting the model's accuracy in capturing solitary wave propagation.

4.2. Variation of velocity within a solitary wave

This case focuses on comparing the simulated velocity field with the corresponding analytical solution derived from Laitone's theory (Laitone, 1960). The configuration and mechanical parameters are

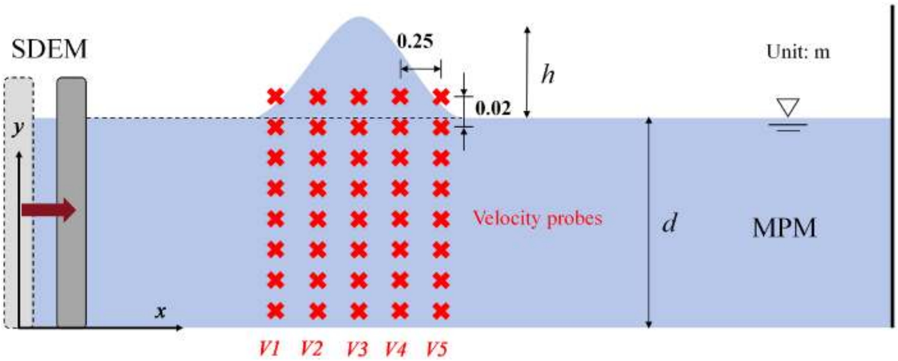

Fig. 8. Layout of the velocity probes within a solitary wave.

consistent with those used in the previous example. The simulation runs the same time as the previous validation case. As illustrated in Fig. 8, five arrays of velocity probes (i.e., $V1$-$V5$) are strategically positioned to record velocities at various horizontal and vertical locations during the propagation of the solitary wave (He et al., 2021). Probe array $V3$ is positioned along the wave crest, while the remaining four arrays are symmetrically distributed. Within each array, probes are spaced at 0.25 m horizontally and 0.02 m vertically. The horizontal (u_x) and vertical (u_y) components of water particle velocities are compared with second-order analytical solutions derived from Laitone's theory (Laitone, 1960), expressed as follows:

$$\frac{u_x}{\sqrt{gd}} = \frac{h}{d}\left\{1+\frac{h}{d}\left[1-\frac{3}{2}\left(\frac{y}{d}\right)^2\right]\right\}\operatorname{sech}^2(\varphi) - \frac{1}{4}\left(\frac{h}{d}\right)^2\left[7-9\left(\frac{y}{d}\right)^2\right]\operatorname{sech}^4(\varphi), \tag{33}$$

$$\frac{u_y}{\sqrt{gd}} = \sqrt{3}\frac{y}{d}\left(\frac{h}{d}\right)^{3/2}\left\{1+\frac{h}{d}\left[1-\frac{1}{2}\left(\frac{y}{d}\right)^2\right]\right\}\operatorname{sech}^2(\varphi)\tanh(\varphi) - \frac{\sqrt{3}}{2}\frac{y}{d}\left(\frac{h}{d}\right)^{5/2}\left[7-3\left(\frac{y}{d}\right)^2\right]\operatorname{sech}^4(\varphi_2)\tanh(\varphi). \tag{34}$$

where y denotes the vertical coordinate of the probe, and x represents the horizontal coordinate. $\varphi = 2\pi\left(\frac{x}{\lambda} - \frac{t}{T_f}\right) + \pi$ is the wave phase, T_f is the wave period as defined in Eq. (6), and λ is the wavelength.

As shown in Fig. 9, the up subplot is the comparison of numerical and analytical results for horizontal velocities, and the bottom subplot is the non-dimensional horizontal velocity distribution across the Probe array range, with V1-V5 indicating the probe array locations. The horizontal velocities are normalized by the shallow water wave celerity $\sqrt{gd}$ (Winckler Grez, 2021), which is consistent with the scaling presented in the Eq. (33). The horizontal velocity distribution of a solitary wave is symmetric about the crest, with nearly identical magnitudes observed at equidistant points ahead of and behind the crest. The horizontal velocity decreases progressively from the crest in both directions. Moreover, at the crest, surface water particles exhibit higher horizontal velocities than those near the bottom. This occurs because the upper layer fluid particles encounter less restriction to motion. Conversely, the lower layers are affected more by greater constraints, such as increased hydrostatic pressure and bottom friction, which lead to a reduction in flow velocities. This occurs because the upper layer experiences stronger acceleration due to the free surface condition, which allows for less friction and a more pronounced pressure gradient. However, the lower layer is affected by bottom friction, resulting in slower velocities.

Fig. 10 shows the spatial distribution of vertical velocities, demonstrating a symmetric pattern with respect to the solitary wave crest. The vertical velocities are normalized by the shallow water wave celerity $\sqrt{gd}$ (Winckler Grez, 2021), which is consistent with the scaling presented in the Eq. (34). The up subplot is the comparison of numerical and analytical results for vertical velocities, and the bottom subplot is the non-dimensional vertical velocity distribution across the Probe array range, with V1-V5 indicating the probe array locations. Unlike the horizontal velocity profile, the vertical components initially decrease and then increase, reaching their maximum near the crest. This peak is

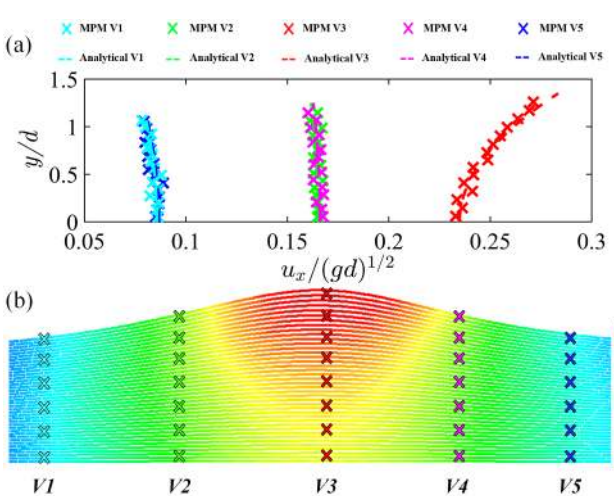

Fig. 9. (a) Comparison between numerical and analytical solutions of horizontal velocities at $t = 3$ s. (b) Non-dimensional horizontal velocity distribution across the probe array at $t = 3$ s, with V1-V5 indicating the probe locations.

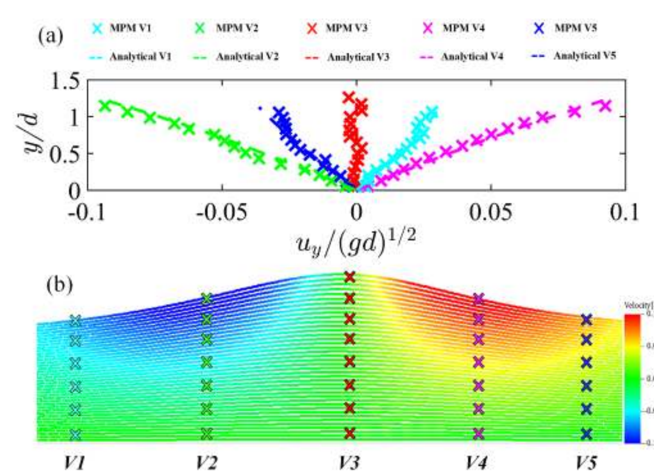

Fig. 10. (a) Comparison between numerical and analytical solutions of vertical velocities at $t = 3$ s. (b) Non-dimensional vertical velocity distribution across the probe array at $t = 3$ s, with V1-V5 indicating the probe locations.

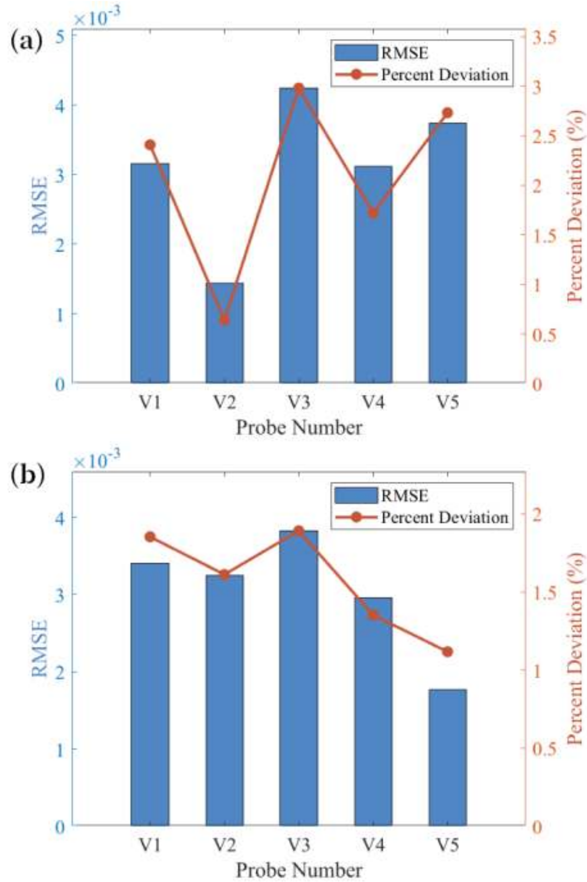

Fig. 11. RMSE and percent deviation of variation of velocity within a solitary wave. (a) is the horizontal velocity, (b) is the vertical velocity.

caused by the steep gradient of the free surface, which generates strong pressure differences that vertically accelerate the fluid. Additionally, water particles ahead of the crest exhibit upward motion as the wave approaches, while those behind the crest switch to downward motion as the wave passes. At the wave crest position, the vertical velocity is nearly zero, corresponding to the instant when water particles reach their highest elevation and momentarily shift from upward to downward movement.

Figs. 9 and 10 show that the numerical results closely match the analytical solutions for both horizontal and vertical velocity distributions. This agreement validates the accuracy and robustness of the proposed coupling method in capturing the velocity variations within the solitary wave.

As presented in Fig. 11, both horizontal and vertical velocity components were evaluated at five probe locations (V1-V5), the upper plot is the horizontal velocity, the lower plot is the vertical velocity. The RMSE for horizontal velocity ranges from 1.4×10^{-3} to 4.3×10^{-3}, with the largest error at V3; percent deviations vary between 0.88 % and 3.12 %. Vertical velocity shows smaller discrepancies, with RMSE values between 1.8×10^{-3} and 3.9×10^{-3}, indicating reliable prediction of internal velocity.

Fig. 12 presents the time series of velocity at selected locations. Data are extracted at three horizontal positions (3.5 m, 5.5 m, and 7.5 m from the wave maker) and at three vertical levels (bottom, middle, and top) at each location. It is evident that the velocity decreases with increasing distance from the wave maker, which can be attributed to the inclusion of viscous effects in the numerical simulations. Additionally, velocities near the bottom are also lower than those in the upper layers, reflecting stronger constraints and boundary effects near the bed, consistent with the spatial velocity distributions presented earlier.

Lastly, in the current MPM scheme, the fluid pressure is computed based on a weakly compressible equation of state, which can lead to visible pressure oscillations. One potential solution is to adopt an incompressible MPM formulation, as suggested in previous studies (Zhang et al., 2017). Despite these oscillations, the numerical results across all validation cases exhibit good agreement with theoretical predictions and experimental data.

4.3. Solitary wave run-up on a vertical wall

In this case, the geometric layout differs from the previous examples, but the mechanical parameters remain unchanged. As depicted in Fig. 13, the flume is 2.5 m long and the water depth is 0.20 m. The numerical simulations run on Intel Core™ i9-14900K (10 cores), which took about 0.41 h of runtime. The solitary wave run-up height is recorded at the end of the flume, where a fixed vertical wall is positioned. In this case, the fixed vertical wall is also modeled using SDEM element, allowing for a consistent implementation of the spring-dashpot contact model between the water and the solid boundary.

To further validate the predictive capability of the proposed coupling framework, Fig. 14 compares the normalized run-up height (R/d) as a function of normalized wave height (h/d) across various numerical models and experimental data. The experimental measurements from Chan and Street (1970) serve as the benchmark. The results provided by the MPM-SDEM coupling implemented in this manuscript agree closely with the experimental trend and show comparable or improved performance relative to established methods.

Greater initial wave heights lead to increased run-up at the vertical wall, as illustrated in Fig. 14. The height of the vertical climb is directly related to the initial energy of the solitary wave, which is primarily governed by its height. As the wave propagates, its kinetic energy is progressively transformed into potential energy due to the upward forcing effect of the wall. The vertical wall reflects the wave's momentum, driving the water mass upward along its surface. However, the relationship between the normalized wave height (h/d) and normalized run-up height (R/d) is non-linear, owing to the intrinsic non-linearity of the solitary waves.

The RMSE and percent deviation between the numerical and experimental results are shown in Fig. 15, demonstrating a consistent upward trend with increasing relative wave height h/d. Specifically, RMSE values increase from 0.0135 at $h/d = 0.2$ to 0.0366 at $h/d = 0.6$, while the corresponding percent deviation grows from 0.87 % to 3.65 %. This trend indicates that the accuracy of the run-up prediction decreases for larger waves, which is likely due to enhanced non-linear effects and increased energy dissipation near the wall. Nevertheless, the relatively low error values confirm that the model's reliable reproduction of run-up dynamics across a range of wave amplitudes.

A sensitivity analysis was performed on the key contact parameters focusing on cases with h/d of 0.3, specifically the normal stiffness (k_n), normal damping (g_n), and tangential damping (g_t). The impact of varying these parameters over a representative range was evaluated in terms of resulting wave run-up error. As shown in Table 3, the maximum error variation across all parameters remains below 0.17 %, indicating that the model exhibits low sensitivity to these values within the considered

Table 3
Sensitivity analysis of the key contact parameters.

$k_n(kg/s^2)$	250	350	550	650
Error	0.0156 %	0.0137 %	0.0149 %	0.0128 %
$g_n(kg/s)$	0.05	0.1	0.2	0.25
Error	0.0152 %	0.0126 %	0.0143 %	0.0127 %
$g_t(kg/s)$	5.0×10^{-8}	5.0×10^{-7}	5.0×10^{-5}	5.0×10^{-4}
Error	0.1698 %	0.0826 %	0.0793 %	0.1537 %

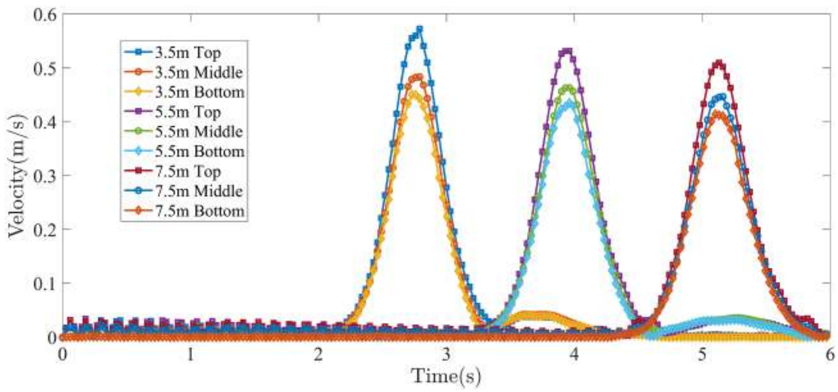

Fig. 12. Time series of the velocity computations at selected locations.

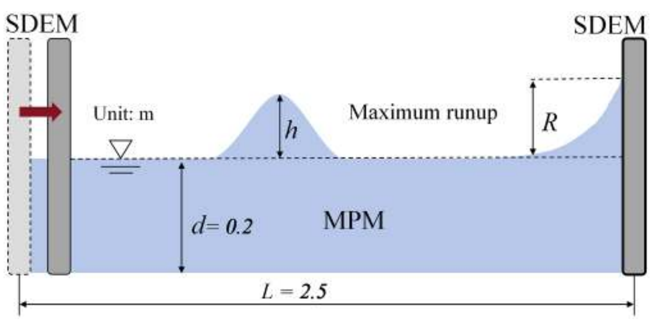

Fig. 13. Setup of the wave running up a vertical wall.

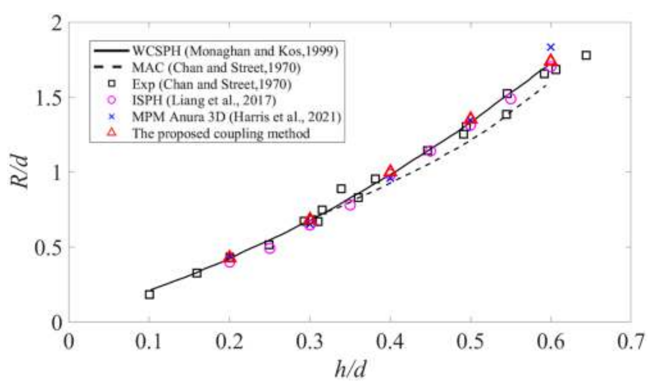

Fig. 14. Comparison of normalized run-up height R/d versus normalized wave height h/d among various numerical methods and experimental data. WCSPH: Weakly-Compressible Smoothed Particle Hydrodynamics (Monaghan, 1994); MAC: Marker and Cell method (Chan and Street, 1970); Exp: Experimental data (Chan and Street, 1970); ISPH: Incompressible Smoothed Particle Hydrodynamics (Liang et al., 2017); MPM Anura 3D (Harris et al., 2021).

range. Given the difficulty of directly measuring these parameters, they were carefully calibrated against experimental data to ensure optimal agreement.

4.4. Solitary wave impact loading on a vertical wall

The impact force exerted by a solitary wave is a critical consideration for the design of seawall structures. In this section, some normalized wave heights (h/d) are considered to evaluate the influence of the wave impact forces on the wall. The geometrical configuration of the flume and the mechanical parameters implemented for this numerical simulation are identical to those described in Section 4.3. The numerical simulations run on Intel Core™ i9-14900K (10 cores), which took about 0.33 h of runtime.

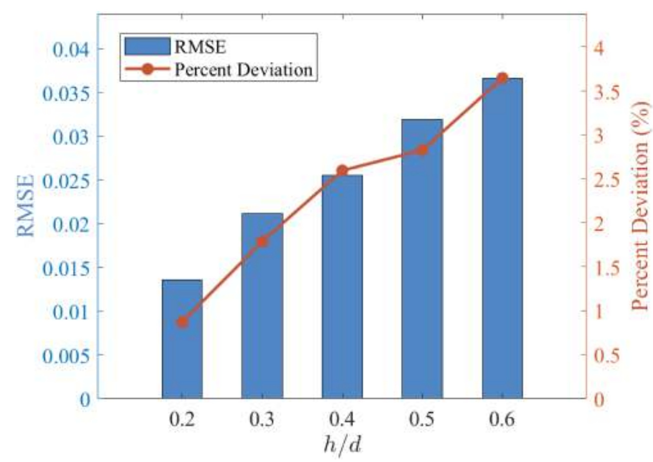

Fig. 15. RMSE and percent deviation of solitary wave run-up on a vertical wall.

4.4.1. Semi-analytical results comparison

This case focuses on comparing the simulated velocity field with the corresponding semi-analytical solution derived from the work of Cooker et al. (1997). Fig. 16 presents the normalized wave impact forces on the vertical seawall. The total impact force on the structure is derived by summing all coupling forces from MPM particles to the SDEM wall, where each coupling force includes both normal and tangential components, as defined in Eqs. (28) and (29). To quantitatively analyze the wave impact loading, six cases with different normalized wave heights (ranging from 0.1 to 0.6) are examined. The results are compared with those obtained using the boundary-integral method proposed by Cooker et al. (1997).

The results are presented in Fig. 16(a) for smaller normalized wave heights ($h/d = 0.1$ to 0.3) and in Fig. 16(b) for larger heights ($h/d = 0.4$ to 0.6). In these figures, $\tau = (t - t_0)\sqrt{g/d}$ is used for time normalization, where d and g represent initial still water depth and gravitational acceleration, respectively. t_0 denotes the time instant of maximum wave run-up. The computed normalized impact forces demonstrates satisfactory agreement with Cooker's results, thereby validating the accuracy of the present model.

The results reveal a strong dependence of the impact forces on the normalized wave height. Specifically, when $h/d < 0.4$, the impact forces exhibit a single peak, occurring approximately at the time of maximum wave run-up. In contrast, when $h/d > 0.4$, the impact forces transitions to a double-peak pattern. The initial peak is attributed to the direct impact of the wave, while the subsequent peak arises during the wave's

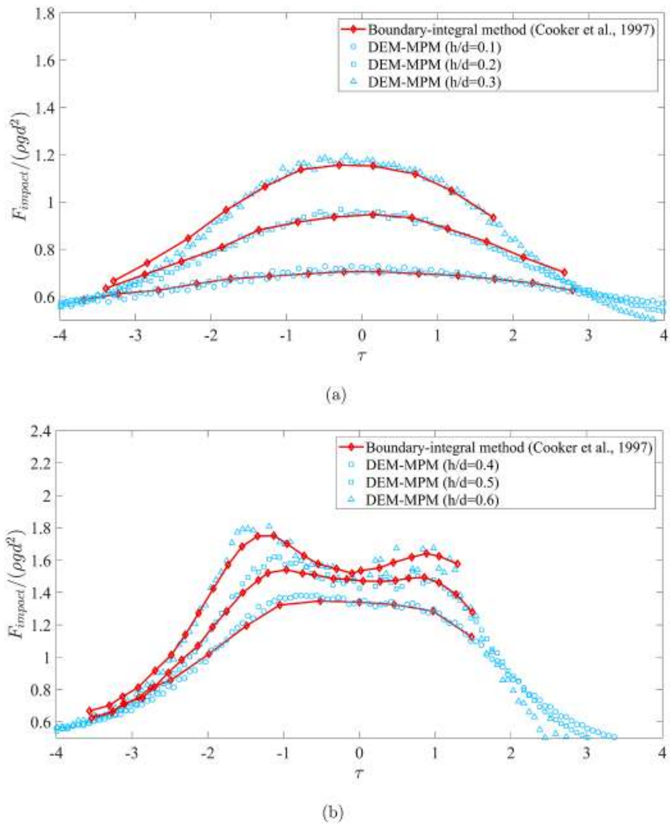

Fig. 16. (a) Solitary wave impact forces for $h/d = 0.1 - 0.3$, and (b) solitary wave impact forces for $h/d = 0.4 - 0.6$.

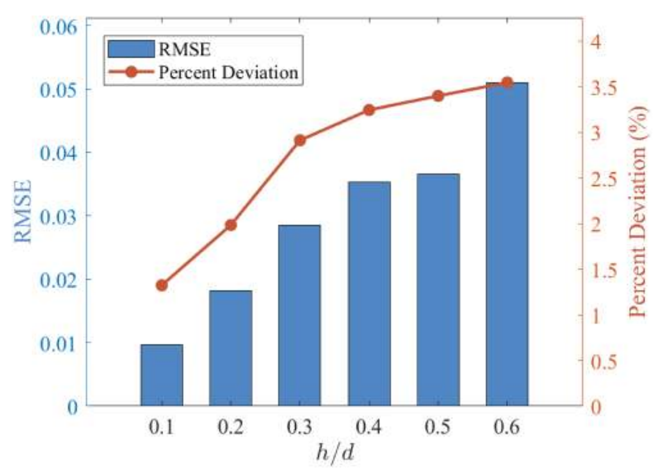

Fig. 17. RMSE and percent deviation of solitary wave impact loading on a vertical wall.

retreat. This transition in force behavior underscores the substantial influence of wave height on the characteristics of the impact loading.

As shown in Fig. 17, both RMSE and percent deviation increase with the normalized wave height h/d. The RMSE rises from 0.0097 at $h/d = 0.1$ to 0.0512 at $h/d = 0.6$, with percent deviation peaking at 3.52 %, demonstrating acceptable agreement in predicting impact force magnitudes.

4.4.2. Experimental results comparison

An experiment conducted by Hess et al. (2023) was reproduced for comparison with the numerical results. In the experiment, a vertical wall was installed at a location 4.35 m from the center of the wave maker.

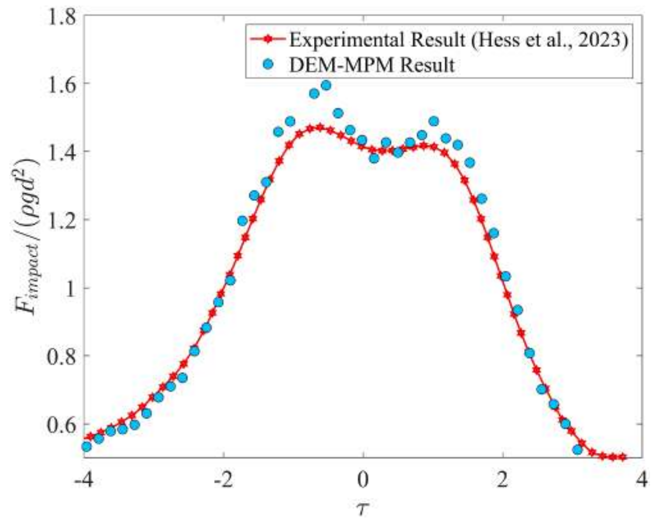

Fig. 18. The instantaneous wave force as function of time for h = 0.3 m and d = 0.15 m.

Table 4
RMSE and percent deviation of impact force comparison with experiment.

	RMSE	Percent Deviation
h/d = 0.5	0.0496	3.9227 %

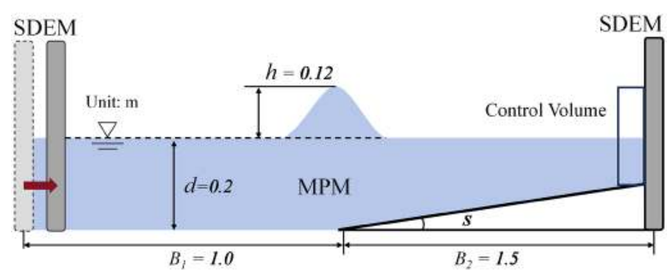

Fig. 19. Setup of a solitary wave propagating over a sloping bathymetry.

The water depth was set to 0.30 m, and the wave amplitude was 0.15 m. The numerical setup is identical to that of the experiment. In the MPM, a mesh resolution of $0.01\ \mathrm{m} \times 0.01\ \mathrm{m} \times 0.01\ \mathrm{m}$ was used, with four particles per cell. The mechanical parameters remained consistent with those used in the previous case, as listed in Table 2.

As shown in Fig. 18, two distinct peaks appear in the loading history during the impact of a solitary wave on the vertical wall when the normalized wave height exceeds 0.4. This phenomenon can be attributed mainly to the steepened wave front associated with higher wave amplitudes. The first peak arises from the initial impact of the wave front, while the second peak is likely caused by the interaction between the wave tail and the reflected wave. The numerical results capture this trend well, although the first peak is slightly overestimated. This overestimation may be due to numerical artifacts inherent to the MPM, as previous studies have reported that MPM can exhibit numerical noise when dealing with large deformations (Zhao and Choo, 2020; Chen et al., 2018). Overall, the numerical results show acceptable agreement with the experimental data, demonstrating the accuracy and reliability of the proposed numerical framework.

Furthermore, the RMSE and percent deviation are listed in Table 4, yielding an RMSE of 0.0496 and a percent deviation of 3.9227 %.

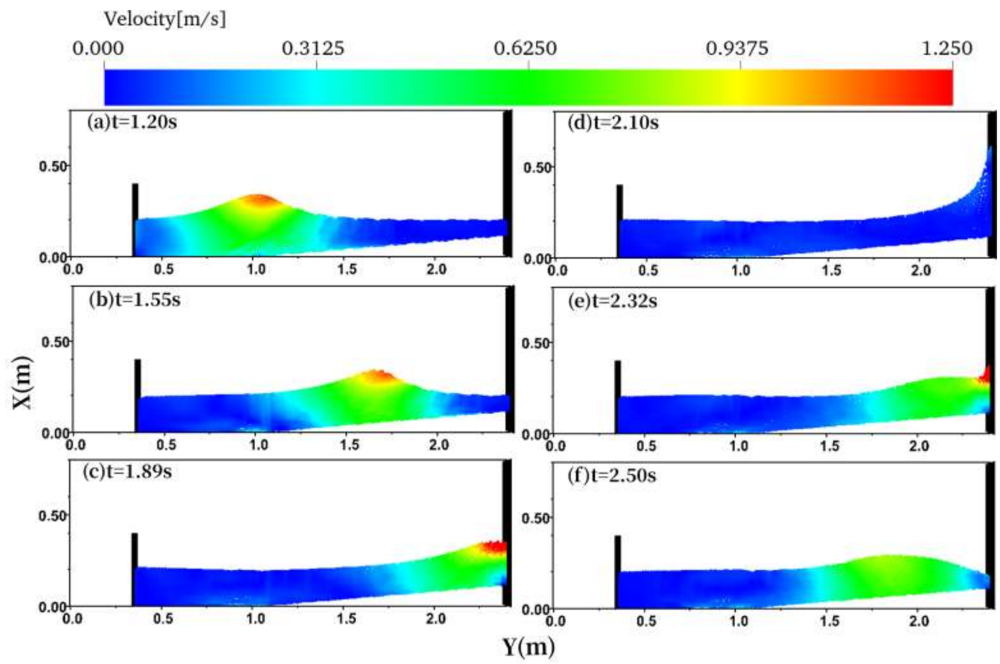

Fig. 20. Wave-structure interaction at different stages with a slope of $s = 1/15$.

5. Solitary wave interacting with sloping bathymetry and seawall

Understanding how waves interact with seawall structures is essential, especially considering the dynamic forces involved. To gain deeper insights, comprehensive simulations are conducted to examine the effects of varying beach slopes on wave-structure interactions. Fig. 19 illustrates a solitary wave propagating over a sloping bathymetry. The geometric parameters are defined as follows: B represents the horizontal length of the flat bottom, and s denotes the slope, expressed as the vertical rise per unit of horizontal run. Three different slopes are evaluated (namely $s = 1/10, s = 1/12, s = 1/15$). The numerical simulations run on Intel Core™ i9-14900K (10 cores), which took about 0.21 h of runtime. The mechanical parameters used are consistent with those described in Section 4.3.

5.1. Evolution of water-structure interaction

Fig. 20 shows time histories of the evolution of wave-structure interaction for the case of $s = 1/15$. The propagation of the solitary wave on the slope is divided into three distinct stages. In the first stage (from a to b), the solitary wave propagates along the slope following its initial generation. As the water depth decreases, the wave height increases in accordance with the principle of conservation of energy. The second stage (from c to d) involves the interaction between the solitary wave and the seawall. Upon reaching the seawall, the wave begins to interact with the structure. The leading part of the wave is influenced by the reaction force from the seawall, causing the wave to deform gradually, with the wave height continuing to rise as it ascends the seawall. During this phase, surging-type wave breaking occurs, where the wave primarily exerts thrust on the seawall. The third stage (from e to f) represents the wave retreat phase. After the wave reaches its peak, back-flow develops, and the water begins to flow in the opposite direction, resulting in reversed wave motion.

5.2. Wave velocity and load

To quantitatively analyze the velocity evolution of the solitary wave along the slope, a control volume, extending twice the background grid size in the x-direction, is used to compute the average velocity magnitude, $\bar{V}$. Fig. 21 illustrates the relationship between the normalized wave velocity, which is expressed through the Froude number $F_r = \bar{V}/\sqrt{gh}$, and the slope angle plotted as a function of the normalized time, $t\sqrt{g/h}$, using the wave height. As time progresses, the velocity gradually increases, reaching a maximum at approximately time 13.5. Subsequently, the velocity decreases approaching zero before rising again to a second higher peak. Notably, as the slope angle increases, the magnitude of the velocity peaks also increases. The variation in wave velocity is primarily influenced by factors such as slope angle, water depth, and energy dissipation. It is possible to see that the slope angle plays a dominant role since steeper slopes accelerate the transformation of potential energy into kinetic energy, thereby amplifying the magnitude of the velocity peaks.

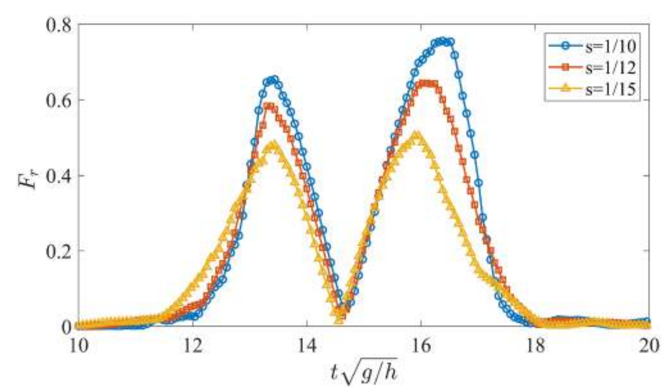

Fig. 21. Normalized wave velocity as a function of the normalized time for different slope angles.

5.3. Relationship between the velocity and load

Fig. 22 illustrates the relationship between the normalized wave velocity and the number of water points within the control volume. The data indicate that velocity initially increases and then decreases as the number of points grows. When the number of points reaches its maxi-

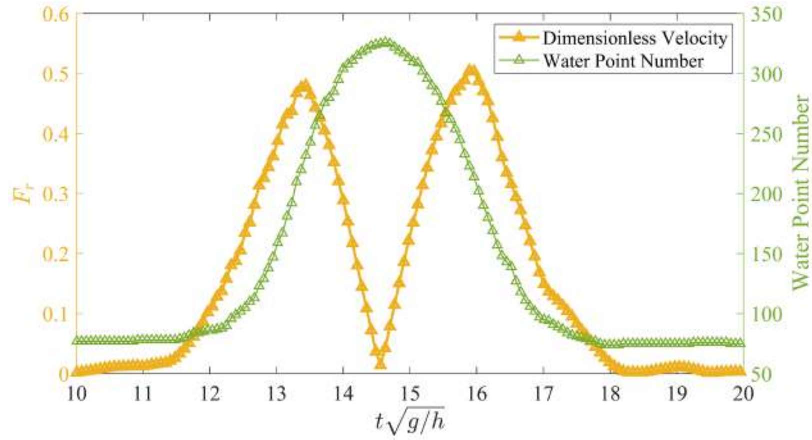

Fig. 22. Evolution of the normalized average velocity and discretization refinement (number of water points) as functions of normalized time.

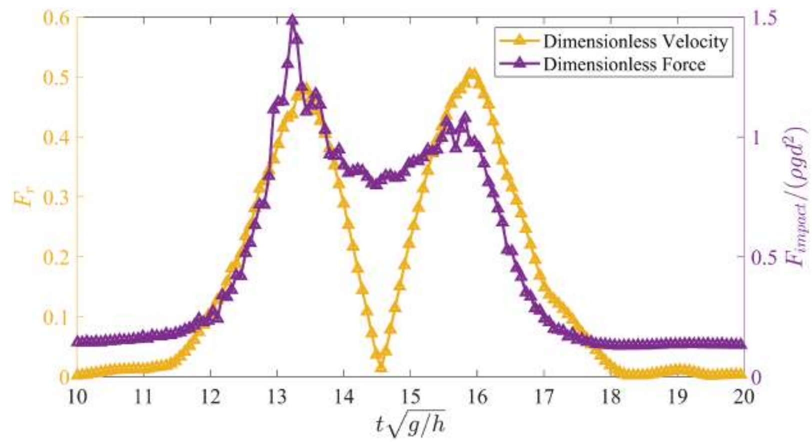

Fig. 23. Evolution of the normalized average velocity and impact force as a function of the normalized time.

mum, the velocity attains its minimum. At this stage, the wave reaches its crest (as shown in Fig. 20(d)), and the kinetic energy of the wave is converted into potential energy. Subsequently, the wave enters the retreat phase, during which the number of points in the control area gradually decreases. As a result, the velocity increases again, reaching a secondary peak before decreasing once more.

To further examine the relationship between velocity and the impact force, Fig. 23 shows the variation of the normalized wave velocity and force over time. A strong correlation between the two is evident, with both exhibiting similar patterns of increase and decrease, maintaining consistent alignment throughout the simulation. The first force peak is higher than the second, corresponding to the significant interaction between the wave and the seawall. During this phase, the wave exerts substantial force on the seawall while continuing to ascend. The second peak occurs as a result of the wave's backflow, where the reverse water movement impacts the seawall, generating an additional smaller force. Notably, the occurrence of two force peaks is commonly observed in high-ratio scenarios, as shown in Fig. 16(b). In contrast, the wave amplitude remains relatively small in lower ratio cases, limiting the wave's ascent and preventing the development of a significant backflow impact force.

6. Conclusion

A coupled MPM-SDEM scheme has been developed to simulate solitary wave generation and its interaction with fixed or movable boundaries in coastal applications. By implementing the MPM for representing the fluid, the framework effectively handles large deformations and moving free surfaces without mesh distortion. Meanwhile, the SDEM accurately represents the geometry and movement of wave-makers and other structures. The coupling is achieved via a DEM-based contact algorithm that calculates normal and tangential contact forces at fluid-structure boundaries.

Extensive validation against benchmark problems shows that the proposed method successfully captures wave propagation, run-up, reflection, and impact loads on vertical walls, matching experimental measurements and established theoretical solutions. The results confirm that wave height, slope angle, and wave steepness play key roles in run-up height and impact loads. For larger normalized wave heights, a two-peak loading pattern often emerges due to direct impact and subsequent backflow. The analyses also reveal how velocity fields correlate with force evolution, contributing to a clearer understanding of the physics behind wave-structure interactions.

Overall, this study introduces an advanced MPM-SDEM coupling framework that incorporates a physically consistent elastic spring-dashpot contact model to resolve interactions between fluid and solid phases. By accurately capturing complex processes such as solitary wave generation, run-up, and structure impact forces, the proposed framework not only enhances numerical fidelity but also offers a promising tool for coastal infrastructure design and hazard mitigation. Its rigorous validation highlights its robustness and versatility in simulating nonlinear wave-structure interactions.

CRediT authorship contribution statement

Songkai Ren: Writing – original draft, Visualization, Validation, Software, Methodology, Investigation, Formal analysis, Conceptualization; **Zhuo Liu:** Writing – original draft, Visualization, Validation, Resources, Investigation, Formal analysis; **M.G. Trujillo-Vela:** Writing – review & editing, Formal analysis, Conceptualization; **S.A. Galindo-Torres:** Writing – review & editing, Supervision, Conceptualization; **Xiaoqing Tian:** Writing – review & editing, Supervision, Software, Funding acquisition, Conceptualization; **Pei Zhang:** Writing – review & editing, Supervision, Methodology, Funding acquisition.

Declaration of competing interest

The authors declare that they have no known competing financial interests or personal relationships that could have appeared to influence the work reported in this paper.

Acknowledgement

We gratefully acknowledge the funds from Zhejiang Province Leading Goose Plan Project (No. 2025C02017) , Scientific Research Starting Fund from Hangzhou Dianzi University (No. KYS015624320), National Natural Science Foundation of China (No. 12172305), project supported by SKL of HESS. We thanks Westlake University Supercomputer Center for computational resource and related assistance. The presented simulations were conducted based on the ComFluSoM open source library (https://github.com/peizhang-cn/ComFluSoM).

Supplementary material

Supplementary material associated with this article can be found in the online version at 10.1016/j.oceaneng.2025.122195.

References

Altomare, C., Scandura, P., Cáceres, I., Viccione, G., et al., 2023. Large-scale wave breaking over a barred beach: SPH numerical simulation and comparison with experiments. Coastal Eng. 185, 104362.
Bardenhagen, S.G., Mm, K.E., 2004. The generalized interpolation material point method. Comput. Model. Eng. Sci. 5 (6), 477–496.
Bisht, V., Salgado, R., Prezzi, M., 2021. Simulating penetration problems in incompressible materials using the material point method. Comput. Geotech. 133, 103593.
Chan, R. K.-C., Street, R.L., 1970. A computer study of finite-amplitude water waves. J. Comput. Phys. 6 (1), 68–94.
Chen, Y.-k., Meringolo, D.D., Liu, Y., 2024. SPH Numerical model of wave interaction with elastic thin structures and its application to elastic horizontal plate breakwater. Mar. struct. 93, 103531.
Chen, Z.-P., Zhang, X., Sze, K.Y., Kan, L., Xin-Ming, Q., 2018. v-p material point method for weakly compressible problems. Comput. Fluids 176, 170–181.
Cooker, M.J., Weidman, P.D., Bale, D.S., 1997. Reflection of a high-amplitude solitary wave at a vertical wall. J. Fluid Mech. 342, 141–158.
De Vaucorbeil, A., Nguyen, V.P., Sinaie, S., Wu, J.Y., 2020. Material point method after 25 years: theory, implementation, and applications. Adv. Appl. Mech. 53, 185–398.
Domínguez, J.M., Altomare, C., Gonzalez-Cao, J., Lomonaco, P., 2019. Towards a more complete tool for coastal engineering: solitary wave generation, propagation and breaking in an SPH-based model. Coastal Eng. J. 61 (1), 15–40.
Fu, T., Feng, D., Yin, J., Yi, C., Chen, J., 2024. Multi-dimensional modeling of solitary wave–structure interaction problems by using a δ-LES-SPH model. Eng. Anal. Bound. Elem. 169, 105965.
Galindo-Torres, S.A., Pedroso, D.M., Williams, D.J., Li, L., 2012. Breaking processes in three-dimensional bonded granular materials with general shapes. Comput. Phys. Commun. 183 (2), 266–277.
Goring, D.G., Raichlen, F., 1979. Tsunamis, the propagation of long waves onto a shelf. PhD thesis, California Institute of Technology (1979).
Han, X., Dong, S., 2020. Interaction of solitary wave with submerged breakwater by smoothed particle hydrodynamics. Ocean Eng. 216, 108108.
Harris, L., Liang, D., Shao, S., Zhang, T., Roberts, G., 2021. MPM Simulation of solitary wave run-up on permeable boundaries. Appl. Ocean Res. 111, 102602.
He, M., Khayyer, A., Gao, X., Xu, W., Liu, B., 2021. Theoretical method for generating solitary waves using plunger-type wavemakers and its smoothed particle hydrodynamics validation. Appl. Ocean Res. 106, 102414.
Heller, V., 2011. Scale effects in physical hydraulic engineering models. J. Hydraul. Res. 49 (3), 293–306.
Hess, F., Boes, R.M., Evers, F.M., 2023. Forces on a vertical dam due to solitary impulse wave run-up and overtopping. J. Hydraul. Eng. 149 (7), 04023020.
Hsiao, S.-C., Hsu, T.-W., Lin, T.-C., Chang, Y.-H., 2008. On the evolution and run-up of breaking solitary waves on a mild sloping beach. Coastal Eng. 55 (12), 975–988.
Jose, J., Choi, S.-J., Giljarhus, K. E.T., Gudmestad, O.T., 2017. A comparison of numerical simulations of breaking wave forces on a monopile structure using two different numerical models based on finite difference and finite volume methods. Ocean Eng. 137, 78–88.
King, J.R.C., Lind, S.J., Rogers, B.D., Stansby, P.K., Vacondio, R., 2023. Large eddy simulations of bubbly flows and breaking waves with smoothed particle hydrodynamics. J. Fluid Mech. 972, A24.
Korteweg, D.J., de Vries, G., 1895. On the change of form of long waves advancing in a rectangular canal, and on a new type of long stationary waves. Philos. Mag. 39 422-443.
Krautwald, C., Von Haefen, H., Niebuhr, P., Voegele, K., Schuerenkamp, D., Sieder, M., Goseberg, N., 2022. Large-scale physical modeling of broken solitary waves impacting elevated coastal structures. Coastal Eng. J. 64 (1), 169–189.
Kularathna, S., Liang, W., Zhao, T., Chandra, B., Zhao, J., Soga, K., 2021. A semi-implicit material point method based on fractional-step method for saturated soil. Int. J. Numer. Anal. Methods Geomech. 45 (10), 1405–1436.
Laitone, E.V., 1960. The second approximation to cnoidal and solitary waves. J. Fluid Mech. 9, 430-444.
Lei, X., Chen, X., Yang, Z., He, S., Zhu, L., Liang, H., 2022. A simple and robust MPM framework for modelling granular flows over complex terrains. Comput. Geotech. 149, 104867.
Lei, Z., Zhou, J., Zhang, Z., Zhang, J.-M., Jie, Y., Wu, B., 2024. Hydrodynamic responses of the triangle-shaped semi-submersible platform under wave loadings by an incompressible material point method and finite element method model. Ocean Eng. 312, 119152.
Li, J., Wang, B., Wang, D., Zhang, P., Vardon, P.J., 2023. A coupled MPM-DEM method for modelling soil-rock mixtures. Comput. Geotech. 160, 105508.
Lian, Y.P., Zhang, X., Liu, Y., 2012. An adaptive finite element material point method and its application in extreme deformation problems. Comput. Methods Appl. Mech. Eng. 241, 275–285.
Liang, D., Jian, W., Shao, S., Chen, R., Yang, K., 2017. Incompressible SPH simulation of solitary wave interaction with movable seawalls. J. Fluids Struct. 69, 72–88.
Lind, S.J., Rogers, B.D., Stansby, P.K., 2020. Review of smoothed particle hydrodynamics: towards converged Lagrangian flow modelling. Proc. Royal Soc. A 476 (2241), 20190801.
Liu, C., Sun, Q., Zhou, G. G.D., 2018. Coupling of material point method and discrete element method for granular flows impacting simulations. Int. J. Numer. Methods Eng. 115 (2), 172–188.
Liu, X., Lin, P., Shao, S., 2015. ISPH wave simulation by using an internal wave maker. Coastal Eng. 95, 160–170.
Liu, X., Liu, Y., Lin, P., Wang, D., 2023. Experimental and numerical studies of solitary wave interaction with perforated caisson breakwaters. Phys. Fluids 35, 057119.
Luding, S., 2008. Introduction to discrete element methods: basic of contact force models and how to perform the micro-macro transition to continuum theory. Eur. J. Environ. Civ. Eng. 12 (7-8), 785–826.
Luo, M., Khayyer, A., Lin, P., 2021. Particle methods in ocean and coastal engineering. Appl. Ocean Res. 114, 102734.
Madsen, P.A., Fuhrman, D.R., Schäffer, H.A., 2008. On the solitary wave paradigm for tsunamis. J. Geophys. Res. Oceans 113, C12012.
Man, T., Zhang, P., Ge, Z., Galindo-Torres, S.A., Hill, K.M., 2023. Friction-dependent rheology of dry granular systems. Acta Mech. Sin. 39 (1), 722191.
Meucci, A., Young, I.R., Hemer, M., Kirezci, E., Ranasinghe, R., 2020. Projected 21st century changes in extreme wind-wave events. Sci. Adv. 6 (24), eaaz7295.
Monaghan, J.J., 1994. Simulating free surface flows with SPH. J. Comput. Phys. 110 (2), 399–406.
Monaghan, J.J., 2005. Smoothed particle hydrodynamics. Rep. Prog. Phys. 68 (8), 1703.
Ni, R., Li, J., Zhang, X., Zhou, X., Cui, X., 2022. An immersed boundary-material point method for shock-structure interaction and dynamic fracture. J. Comput. Phys. 470, 111558.
Pan, S., Yamaguchi, Y., Suppasri, A., Moriguchi, S., Terada, K., 2021. MPM–FEM Hybrid method for granular mass–water interaction problems. Comput. Mech. 68 (1), 155–173.
Ren, S., Zhang, P., Galindo-Torres, S.A., 2022. A coupled discrete element material point method for fluid–solid–particle interactions with large deformations. Comput. Methods Appl. Mech. Eng. 395, 115023.
Ren, S., Zhang, P., Man, T., Galindo-Torres, S.A., 2023a. Numerical assessments of the influences of soil–boulder mixed flow impact on downstream facilities. Comput. Geotech. 153, 105055.
Ren, S., Zhang, P., Zhao, Y., Tian, X., Galindo-Torres, S.A., 2023b. A coupled metaball discrete element material point method for fluid–particle interactions with free surface flows and irregular shape particles. Comput. Methods Appl. Mech. Eng. 417, 116440.
Shi, Y.H., Guo, N., Yang, Z.X., 2024. GeoTaichi: a taichi-powered high-performance numerical simulator for multiscale geophysical problems. Comput. Phys. Commun. 301, 109219.
Shimizu, Y., Gotoh, H., 2024. Volume-conserved wavy interface boundary for δ-SPH-based numerical wave flume. Coastal Eng. 67(2), 214–31.
Sun, J.-Z., Zou, L., Govender, N., Sun, Z., Yu, Z.-B., Jin, G.-Q., 2024a. Coupling SPH-DEM method for simulating the dynamic response of breakwater structures under severe free surface flow. Powder Technol. 441, 119805.
Sun, Z., Hua, Y., Xu, Y., Zhou, X., 2024b. Simulation of fluid-structure interaction using the density smoothing B-spline material point method with a contact approach. Comput. Math. Appl. 176, 525–544.

Svendsen, I.A., 1974. Cnoidal waves over a gently sloping bottom. Institute of Hydrodynamics and Hydraulic Engineering.
Takashimizu, Y., Kawakami, G., Urabe, A., 2020. Tsunamis caused by offshore active faults and their deposits. Earth Sci. Rev. 211, 103380.
Tao, J., Zheng, Y., Chen, Z., Zhang, H., 2016. Generalized interpolation material point method for coupled thermo-mechanical processes. Int. J. Mech. Mater. Des. 12, 577–595.
Tsuruta, N., Gotoh, H., Suzuki, K., Ikari, H., Shimosako, K., 2019. Development of PARISPHERE as the particle-based numerical wave flume for coastal engineering problems. Coastal Eng. J. 61 (1), 41–62.
Tsuruta, N., Khayyer, A., Gotoh, H., Suzuki, K., 2021. Development of wavy interface model for wave generation by the projection-based particle methods. Coastal Eng. 165, 103861.
Vacondio, R., Altomare, C., De Leffe, M., Hu, X., Le Touzé, D., Lind, S., Marongiu, J.-C., Marrone, S., Rogers, B.D., Souto-Iglesias, A., 2021. Grand challenges for smoothed particle hydrodynamics numerical schemes. Comput. Part. Mech. 8, 575–588.
Wang, J., He, G., You, R., Liu, P., 2018. Numerical study on interaction of a solitary wave with the submerged obstacle. Ocean Eng. 158, 1–14.
Winckler Grez, P., 2021. Introducción al modelado de procesos costeros. Universidad de Valparaíso, Valparaíso, Chile.
Yao, Y., He, F., Tang, Z., Liu, Z., 2018. A study of tsunami-like solitary wave transformation and run-up over fringing reefs. Ocean Eng. 149, 142–155.
Zhang, F., Zhang, X., Sze, K.Y., Lian, Y., Liu, Y., 2017. Incompressible material point method for free surface flow. J. Comput. Phys. 330, 92–110.
Zhang, P., Sun, S., Chen, Y., Galindo-Torres, S.A., Cui, W., 2021. Coupled material point Lattice Boltzmann method for modeling fluid–structure interactions with large deformations. Comput. Methods Appl. Mech. Eng. 385, 114040.
Zhang, P., Zhao, Y., Galindo-Torres, S.A., Chen, Y., Tang, H., Jin, G., Scheuermann, A., Li, L., 2022. Random walk discrete element Lattice Boltzmann model for scalar transport in fluid and particle flows with strict scalar mass conservation. Int. J. Heat Mass. Transf. 187, 122577.
Zhao, E., Dong, Y., Tang, Y., Xia, X., 2021. Performance of submerged semi-circular breakwater under solitary wave in consideration of porous media. Ocean Eng. 223, 108573.
Zhao, S., Zhao, J., Lai, Y., 2020. Multiscale modeling of thermo-mechanical responses of granular materials: a hierarchical continuum–discrete coupling approach. Comput. Methods Appl. Mech. Eng. 367, 113100.
Zhao, X., Bolognin, M., Liang, D., Rohe, A., Vardon, P.J., 2019. Development of in/outflow boundary conditions for MPM simulation of uniform and non-uniform open channel flows. Comput. Fluids 179, 27–33.
Zhao, Y., Choo, J., 2020. Stabilized material point methods for coupled large deformation and fluid flow in porous materials. Comput. Methods Appl. Mech. Eng. 362, 112742.